Recent multimessenger constraints and the anisotropic neutron star

A. Rahmansyah and A. Sulaksono*
Departemen Fisika, FMIPA, Universitas Indonesia, Depok 16424, Indonesia

(Received 13 June 2021; revised 21 October 2021; accepted 2 December 2021; published 17 December 2021)

The impact of anisotropic pressure models in neutron stars (NSs) is increasing their compactness. Therefore, for the relatively soft NS equation of state (EOS), we can still obtain a relatively large maximum mass of NSs and a relatively short canonical NS radius. We systematically study the anisotropic NS properties using a refined EOS. We compare the results with the recent NS multimessenger constraints. We use a relativistic mean-field (RMF) model with the G3 parameter set to calculate the NS core EOSs. The standard SU(3) prescription and hyperon potential depths determine the hyperon coupling constants. We use the inner and outer crusts EOSs from Miyatsu *et al.* [Astrophys. J. **777**, 4 (2013)]. We consider two kinds of EOSs at high densities: one with the maximum speed of sound in NS matter obeying the conformal bound, i.e., $v_s^{\max} = \frac{1}{\sqrt{3}}$ (WHSS) and one without considering this bound (WH). We have found for the WH EOS with $\Delta = -1.8$ that NS properties predicted for an anisotropic NS based on the Horvat *et al.* model [Classical Quantum Gravity **28**, 025009 (2011)] are entirely compatible with recent NS multimessenger constraints. Whether a $2.6M_\odot$ massive compact object observed in the GW190814 event is an anisotropic NS or not, we found that the compact object is not likely an anisotropic NS.

DOI: 10.1103/PhysRevC.104.065805

I. INTRODUCTION

The LIGO and Virgo Collaborations reported two years ago that they detected a gravitational wave signal from a compact binary coalescence. A gravitational wave signal from this event gives the information that the primary component has a mass $M = 23M_\odot$ and the secondary component (object) has a mass $M = 2.6M_\odot$, where $M_\odot$ is the solar mass. The primary component is a black hole (BH). However, the nature of the secondary object is still unclear because of the lack of measured tidal deformations and the absence of electromagnetic counterpart observations consistent with either a neutron star (NS) or a BH. This secondary component object can be the lightest BH, the heaviest NS, or even a new exotic compact object [1]. Many works have reported the possible explanation about the nature of this massive secondary object. Please see the corresponding discussions for examples in Refs. [2–20]. The possibility that the secondary object of the GW190814 event as a massive static or a slowly rotating NS can trigger a lot of discussions about an appropriate kind of EOS of the massive NS that satisfies observational constraints [5,15,16,21–23]. Furthermore, we note that there was a study that discusses the anisotropic pressure an NS could have with such a large mass [14].

Here, we briefly highlight several recent observational constraints on NS properties. For single NSs, massive pulsars such as PSR J0348+0432, PSR J0740+6620, and PSR J1614–2230 measurements[24–28] provided maximum mass constraints of an NS around $2.0M_\odot$. The x-ray measurements of hot spot emissions on the NS surface with the Neutron Star Interior Composition Explorer (NICER) [29] can simultaneously provide information about the mass and radius of selected pulsars. NICER reported two measurements of pulsars' mass and radius. Those are PSR J0030+0451 in 2019 [30–32], and PSR J0740+6620 in 2021 [33,34]. From observation of a binary NS merger through gravitational waves (GWs), GW170817 [35–37] and GW190425 [1], as well as the corresponding electromagnetic (EM) counterparts associated with GW results, namely AT2017gfo and GRB170817A, one can measure the tidal deformability of NSs and extract an NS mass and the corresponding central density information. (Please see the discussions in, for example, Refs. [38–40].) These multimessenger observations data triggered many studies using Bayesian analysis to put consistent constraints on NS properties. (Please see the discussions in, for example, Refs. [41–50].)

It is worth noting that Landry *et al.* [43] used nonparametric analysis of the heavy pulsar combination, the GW170817 and GW190425 combination, and the NICER observation data. The $1.4M_\odot$ NS radius range predicted by Landry *et al.* [43] is $12.32^{+1.09}_{-1.47}$ km. This radius range is compatible with the recent report of $1.4M_\odot$ NS radius range from the NICER Collaboration [33,34]. Breschi *et al.* [42] used Bayesian analysis from AT2017fgo and GW170817 observation data. Note that the $1.4M_\odot$ NS radius range obtained by Breschi *et al.* [42] is 12.2 ± 0.5 km. This result is also in agreement with the corresponding range reported in Ref. [48]. Furthermore, it can be seen that the radius range obtained by Landry *et al.* [43] and the one obtained by Breschi *et al.* [42] are quite compatible with each other. However, the one of Breschi *et al.* [42] has a narrower range than that of Landry *et al.* [43]. Reed

*anto.sulaksono@sci.ui.ac.id

et al. [41] reported recent analysis on the implication of the ^{208}Pb skin thickness measurement of the PREX-II experiment on the $1.4M_\odot$ NS radius. They obtained the $1.4M_\odot$ radius range extracted from these data as about 13.79 ± 0.49 km. This radius range is large relatively compared to the ones of Refs. [42,43]. However, it is also reported in Ref. [46] that the predicted ^{208}Pb skin thickness extracted from astrophysical constraints such as from heavy pulsar masses, GW results from LIGO/Virgo, and NICER favors a smaller value ^{208}Pb skin thickness than that of PREX-II. We also need to note that the most recent NS maximum mass constraint based on genetic algorithm analysis using GW170817 and GW190814 events data [49] within a 2σ confidence level is $M_{\rm TOV} = 2.21^{+0.116}_{-0.123}\,M_\odot$ when all of the physical quantities in the corresponding analysis are in agreement with the observations. They have also concluded that the secondary object in GW190814 was a BH at merger, although it may well have been a rotating NS at some stage during the binary system evolution. A recent study [50] of Annala *et al.* also reported the upper limit for the dimensionless spin of a rigidly rotating NS as $M_{\rm TOV} < 2.53M_\odot$ (or $M_{\rm TOV} < 2.19M_\odot$, if we assume that a massive NS is created).

The assumption that matter is a fluid with local isotropic pressure is common in NS property studies. However, NSs as compact objects with a wide range density—from dilute nonhomogeneous matter of the crust to the homogeneous core with densities larger than twice nuclear saturation density and composed of many kinds of interacting particles—have quite complex structures. Therefore, for a more realistic description of an NS, the simple local isotropic matter description is not too natural. However, the most general spherically symmetric solution to Einstein equations allows for the anisotropy of the principal pressures: the radial pressure can differ from the transverse pressure [51]. It has also been known for a long time that astrophysical objects need not be isotropic. The Einstein cluster geometries are only sustained purely by tangential stresses. This case is a famous example of the crucial role of anisotropic pressure. (Please see Ref. [52] and the corresponding references therein.) Many studies of the crucial impacts of anisotropy in stellar objects were recently reported. The impact anisotropic pressure in brown dwarfs is discussed in Refs. [52,53]. Modeling of anisotropic magnetic white dwarfs with the γ metric is reported in Ref. [54]. Simultaneously, the important role of anisotropic pressure in quark stars is discussed in Ref. [55]. Moreover, we need to note that the scalar field minimally coupled to gravity also yields anisotropic pressure in boson stars [56]. One also can find that anisotropic pressure cannot be avoided in the exotic solutions of Einstein equations such as wormholes and gravastars. (Please see the discussions in Ref. [51] and the corresponding references therein.) Furthermore, some studies have shown that anisotropic stars can be considered as candidates of ultracompact objects within general relativity (GR) [57,58]. For a NS itself, in principle, the realistic EOS should be obtained from matter models that are compatible with all experimental data of the finite nuclei, hypernuclei, and nuclear matter up to intermediate densities. The models can be nonrelativistic or relativistic. Hundreds of EOS models from many approaches have already been proposed so far. One of the known models is the relativistic mean-field (RMF) model. Note that the authors of Ref. [59] analyzed 263 RMF parameter sets with various variants. They have found only 34 RMF parameter sets that satisfy nuclear matter constraints. Moreover, only 15 of the 34 parameter sets predict NS maximum mass around $2.0M_\odot$ in the case of an isotropic NS without hyperons. Furthermore, if hyperons and other exotic particles are included, none of them satisfy the latter constraints (see Ref. [60] and the references therein for details). This issue is known in the literature as the "hyperon puzzle." The recent discussions on the role of hyperons and other exotics and how to deal with the "hyperon puzzle" can be found, e.g., in Refs. [61–72]; see the references therein for completeness. Note that the appearance of hyperons and other exotic particles in a NS is due to the general physical equilibrium requirement for NS matter known as β stability conditions. Therefore, the consequence of massive NSs and the "hyperon puzzle" simultaneously is that we cannot avoid modifying the common assumptions used to describe NSs. In the first case, one can still apply GR and assume the matter is still isotropic; however, one cannot avoid using the rather unphysical assumption that hyperons and other exotics cannot exist in the NS core. The second case is by modifying the matter and/or geometry. The minimal approach for the second situation involves applying GR if the matter is anisotropic. The issue of hydrostatic equilibrium and stability due to radial pulsation and due to cracking or overturning, gravitational collapse, as well as the energy conditions as general requirements for physically meaningful anisotropic fluids spheres, are discussed in Refs. [51,73–81]. Additionally, we need to note that the anisotropic pressure has impacts on other NS properties such as the moment of inertia, tidal deformability, and universal I-Love-Q relations [82–85]. The authors of Ref. [85] found that anisotropy weakly affects the universal relations and does not prevent the use of universal relations in gravitational wave astrophysics or experimental relativity. Additionally, the increase in variability on the universal relations due to pressure anisotropy can affect their use in future x-ray observations of hot spots on rotating compact stars. Moreover, there are also some analytical models to study anisotropic NSs [73,86]. It is reported [86] that the absence of anisotropy in compact object pressure can lead to a solution that is not physically acceptable as the energy density and speed of sound cannot be positive at the origin at the same time. To this end, we quote the statement in Ref. [57], i.e., "in the real world, anisotropic pressures are the rule rather than the exception."

The appearance of anisotropic pressure in astrophysical objects is due to many related factors merged in complex ways. However, it can be broadly categorized into two kinds of sources. The first is due to the novel properties of matter and the dynamics of the objects, such as the rotations, the presence of strong magnetic and strong electric fields, various kinds of phase transition, superfluidity, boson condensations, two fluids of isotropic matters mathematically equivalent to a single anisotropic fluid, anisotropic momentum distribution in the matter, and so on [52,73,75–77,87,88]. The second factor is based on geometrical reasons. The geometrical source appears since modified gravity models with standard EOS can be mapped into GR with a modified EOS. (Please see

the detailed discussions in Refs. [89–92] and the references therein.) For example, the apparent EOS is anisotropic in the Eddington-inspired Born-Infeld (EiBI) gravity model. This fact is demonstrated explicitly in Ref. [89]. The authors of Ref. [90] have also shown that the field equations of the large class of extended theories of any alternative to GR (ETG) can be recast explicitly into Einstein's field equations with an effective momentum energy tensor. This effective momentum energy tensor can be separated into a standard matter momentum energy tensor and an additional geometrical correction term in the form of symmetric tensor $W^{\mu\nu}$. The explicit form of $W^{\mu\nu}$ depends on the specific ETG under consideration, and it can provide an anisotropic EOS-like contribution (see Eq. (21) in Ref. [90]). Furthermore, it is interesting to note that decoupling gravitational sources in GR to generate anisotropic solutions for self-gravitating systems from a perfect fluid was recently discussed in the context of the braneworld scenario. (Please see Ref. [91] and the references therein.) Another mapping example exists in the nonlocal gravity model with a nonlocal elliptic operator with a well-defined inverse, where the nonlocal version of the Einstein equations with standard matter can be mapped onto standard Einstein equations with the modified nonlocal momentum-energy tensor of the matter and the modified EOS can be anisotropic. (Please see the discussions in Refs. [93,94].) Therefore, the combination of RMF EOS with an anisotropic pressure model is sometimes consistent because the anisotropic pressure that appears in an NS can be caused by effective mapping of the geometrical effect in the matter sector in Einstein field equations.

In the previous work, we have systematically investigated the NS properties predicted by three models of anisotropic pressure of a NS with hyperons [82]. The EOS of the core of a NS is calculated using the RMF model with the BSP parameter set where the standard SU(6) prescription and hyperon potential depths are used to determine the hyperon coupling constants. For the crusts, we used the EOS obtained from Miyatsu *et al.* [95]. The results were compared to other calculations, and experimental and observation data such as $2.0M_\odot$ and recent $1.4M_\odot$ NS radius constraints. The results obtained using the DY model with $\Delta \approx -1.15$ were found to be compatible with all constraints used in that work. In this work, we will discuss the NS properties predicted using a refined NS EOS. We calculate the NS EOS using the G3 parameter set where the hyperon contribution with the SU(3) prescription is considered.

The actual value of the upper bound of NS speed of sound v_s is crucial to understanding the NS EOS properties such as the stiffness and the compressibility. However, the speed of sound remains unconstrained because of the NS EOS uncertainty at high densities. Please see Refs. [43,96–99] and the references therein for detailed discussions related to the status of the bound speed of the sound constraint for high-density NS matter. There are two theoretical upper bounds of the speed of sound proposed and discussed in the literature, i.e., the stability and causality bound [100,101] $v_s^{\max} = 1$ and the conformal bound [102,103] $v_s^{\max} = \frac{1}{\sqrt{3}}$. The conformal bound has been demonstrated in several classes of strongly coupled theories with gravity duals and is saturated only in conformal theory. There is a simple argument offered to support this bound [102]. However, the existence of massive NS is in strong tension with this bound [102]. Furthermore, many works recently reported that, to reconcile a small NS deformability reported by GW events and a large NS maximum mass, the speed of sound in NS should be larger than the conformal bound value. Tews *et al*. [104] found that the sound speed value in NS can reach a value closer to the speed of light at a few times of the nuclear saturation densities. Based on the flexible piecewise polytropic EOS model, Alsing *et al*. [105] estimate the upper bound of the maximum speed of sound $v_s^{\max} > 0.63$. Other authors also found that in an NS the speed of sound can be larger than the conformal bound value. (Please see Refs. [97,99,104] and the references therein for recent discussions.) Note that, as shown in Table I of Ref. [99], the $v_s^{\max}$ bound obtained depends on the EOS and NS composition used. The average value of the v_s results of the corresponding 12 EOSs analysed in Ref. [99] is $v_s = 0.77 \pm 0.14$, while the analysis parametric constraint of Landry *et al.* [43] provides $v_s = 0.85^{+0.15}_{-0.29}$. Note that the authors of Ref. [106] investigated the possible mechanism to explain the rapid growth of v_s in NSs. However, The authors of Ref. [107] reported that the upper limit is close to the conformal bound value, i.e., $v_s^{\max} = 0.5749$, by analyzing global properties of NSs using parametrized and model-independent NS EOSs. Therefore, we also consider two types of the equations of state (EOSs) in a high-density region: one with the maximum speed of sound in NS matter obeying the conformal bound i.e., $v_s^{\max} = \frac{1}{\sqrt{3}}$ (WHSS) and one without considering this bound (WH).

We compare the nuclear matter properties predicted by the G3 [108] parameter set with the ones predicted by BSP [64,109], TM1e [110], FSUGarnet [111], and FSU2H [69] parameter sets. We also compare the nuclear matter properties predicted by the G3 parameter set with other theoretical calculations and experimental constraints. We also compared the results of the DY anisotropic model [51] with the ones of the isotropic, BL anisotropic [112], and HB anisotropic models [113]. Furthermore, we compare the NS property results with the most recent multimessenger Bayesian analysis constraints [41–43,49]. Thus, we use a more recent analysis of observation results to constrain the anisotropic model parameter compared to our previous work [76,82]. Additionally, in the present work, we investigate whether the $2.6M_\odot$ massive object observed by the GW190814 event[1] can be an NS, given an anisotropic model. The investigation is done by studying the possibility of reproducing the canonical NS radius constraint from GW17087 and NICER simultaneously and the constraint deduced from the recent PREX-II experiment [41–43] with the $2.6M_\odot$ massive compact object observed by GW190814 [1].

We have organized this paper as follows: In Sec. II, we discuss the EOS structure and the NS composition. In Sec. III, we briefly discuss the anisotropic models used in this work and show the analytic expressions to calculate the mass-radius relation, moment of inertia, and tidal deformability for anisotropic an NS. In Sec. IV, we discuss the results. Finally, the summary of this work is given in Sec. V.

II. NEUTRON STAR MATTER

This section discusses the model used in this work to describe the EOS of NS matter. According to the compactness and the composition of the matter, the NS EOS can be divided into three regions, i.e., inner crust (inCr), outer crust (outCr), and core. We use the RMF model to calculate the core EOS. At the region near the center, the speed of sound of the corresponding NS EOS predicted by the RMF model can exceed the upper bound of the speed of sound deduced from special relativity or QCD calculation. Consequently, a properly treated EOS in this region should be a physical EOS. The composition of the particles in NS is determined from the potential chemical balance, charge neutrality, and baryon density conservation conditions (β-stability conditions). Particularly, the NS EOS can be schematically arranged as follows [96,97]:

$$P(\epsilon) = \begin{cases} P_{\rm outCr}(\epsilon) & \text{for } \epsilon_{\rm min} \leqslant \epsilon \leqslant \epsilon_{\rm outCr}, \\ P_{\rm inCr}(\epsilon) & \text{for } \epsilon_{\rm outCr} < \epsilon \leqslant \epsilon_c, \\ P_{\rm core}(\epsilon) & \text{for } \epsilon_c < \epsilon_{\rm tr}, \\ v_s^2 \times (\epsilon - \epsilon_{\rm tr}) + P_{\rm core}(\epsilon_{\rm tr}) & \text{for } \epsilon > \epsilon_{\rm tr}, \end{cases} \tag{1}$$

where P, ϵ, and $\epsilon_{\rm tr}$ denote NS pressure, NS energy density, and NS core transition energy density, respectively. Values range from the region with the speed of sound less than the upper bound of NS speed of sound v_s to the region with the speed of sound larger than v_s.

In panel (a) of Fig. 1, we show the speed of sound in NS predicted by all parameter sets used in this work without considering hyperons. At high densities, it is evident that they show similar trends. G3, BSP, and FSU2H predict a similar value of the maximum speed of sound, and FSU Garnet and TM1e yield a similar value of the maximum speed of sound. However, the two parameter set values are less than the three others. Generally, the $v_s^{\rm max}$ values are larger than the conformal bound value and are compatible with the ones obtained by other works [99,105]. Note that $v_s^{\rm max} = 0.72$ and it appears at $\rho/\rho_0 \approx 8.5$ for G3 case. It is still smaller than the average value of the constraint from nonparametric analysis [43], i.e., 0.85. However, the error bar or the contour constraint from Ref. [43] is still too loose to constrain the maximum sound speed predicted by G3 and other EOSs, shown in Fig. 1. In panel (b), we can observe from the red line plot, whose value of $v_s^{\rm max}$ is 0.62. It appears at $\rho/\rho_0 \approx 5.7$ for the case of the G3 parameter set with hyperons considered. It means that the hyperons in the NS core decrease the $v_s^{\rm max}$ value. This number is only slightly larger than the conformal bound, i.e., $\frac{1}{\sqrt{3}}$. Furthermore, the value of $v_s^{\rm max}$ of the G3 with hyperon EOS is smaller than the minimal bound obtained by Alsing *et al.* [105], i.e., $v_s^{\rm max} > 0.63$. Based on the above facts, it is not too clear whether or not the conformal bound of the speed of sound in NSs should be violated in the case of the NS with hyperons EOS. Consequently, we consider both cases in this work. If the conformal bound of the speed of sound is violated, we use an EOS of G3 with hyperons (WH), and we denote G3 with hyperons and the treatment of speed of sound (WHSS) as the representative EOS if the conformal bound is preserved. The speed of sound of WHSS and WH EOSs is shown in panel (b) of Fig. 1. At relatively high densities, one can see the various speed of sound predictions of both EOSs, i.e., $\rho/\rho_0 \approx 5$.

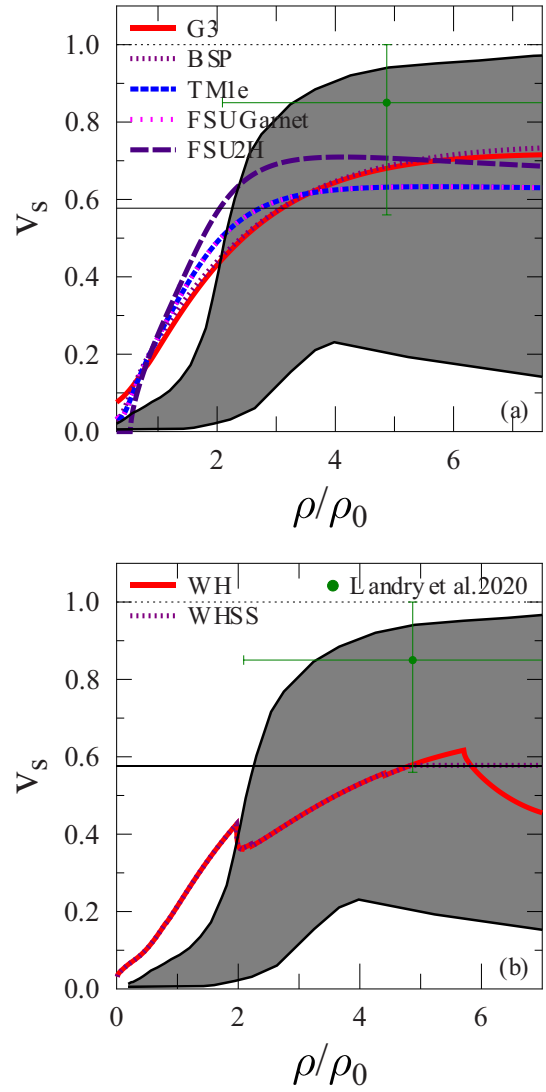

FIG. 1. (a) We show the speed of sound as a function of the density to saturation density ratio, resulting from some RMF parameter sets used in this work if hyperons are excluded. (b) We compare the speed of sound as a function of density to saturation density ratio, resulting from the G3 parameter set with and without hyperons. In (b), WH denote hyperons included, and WHSS denotes the same case as WS but using the conformal bound $v_s^{\rm max} \equiv \frac{1}{\sqrt{3}}$. We insert the constraint from nonparametric analysis [43] denoted as green dot plus the error bars. The gray-shaded area shows the sound contour speed of the 90% credible region for the various combinations of astronomical data. The shaded area is extracted from Ref. [43].

We use the Hartree-Fock Thomas-Fermi model proposed by Miyatsu *et al.* [95] to describe inhomogeneous matter in inCr and outCr of an NS. The inCr and outCr EOSs play a crucial role in the radii and crust thickness of low-mass NSs. Fortin *et al.* reported that prediction error due to the uncertainty of crust EOSs for the NS crust thickness can be as large as 30%, while for the NS radius the uncertainty is about 4% [114]. Note that the benchmark EOS calculation for the

outCr is one of the BPS results [115]. In this result, the masses of finite nuclei are taken from the experimental data atomic mass table of 2003 [116]. The improved outCr EOSs including state-of-the-art theoretical mass tables, which entail pairing effects, effects of deformation, relativistic theoretical nuclear models, and nonrelativistic theoretical nuclear models, have been discussed by Hampel *et al.* [117]. The difference in the outCr thickness of Ref. [117] compared to BPS is about a few percent [118]. Other studies on the outCr of cold nonaccreting neutron stars can be consulted in Refs. [119–121]. The inCr EOSs are obtained using solely theoretical frameworks since the relevant experimental nuclear masses to deduce the corresponding EOS are not available [114]. The theoretical framework commonly used is the compressible liquid-drop model [122] and the Thomas-Fermi approximation [114]. The benchmark calculation of the inCr EOS was done by Bethe [123]. Current developments of inCr EOS have been discussed in Refs. [114,124–127]. Recently, a unified EOS between the crust and the core was proposed. This unified EOS can pin down the uncertainties of NS crust thickness and radius predictions of low-mass NSs [114]. However, The number of RMF parameter sets with unified core-crust EOS available in the literature is only a few. Examples include NL3 [128], NL3$\omega\rho$ [129], GM1 [130], TM1 [131], DDME2 [132], DD2 [133], DDHδ [134], BSR2, and BSR6 [135,136] parameter sets. The ones of the nonrelativistic models can be seen in Table IV of Ref. [114]. To this end, we must point out that by comparing the inCr and outCr EOS calculations by Miyatsu *et al.* [95] with the one calculated by unified EOS, the error can be estimated to about 1% for radius and about 10% for the crust thickness [82].

To describe homogeneous matter in the NS core, we use the RMF model. The expression of the RMF Lagrangian density is [64]

$$\mathcal{L} = \mathcal{L}_{BM} + \mathcal{L}_M + \mathcal{L}_M^{NL} + \mathcal{L}_L. \tag{2}$$

$\mathcal{L}_{BM}$ is the Lagrangian density for baryons ($B = N, \Lambda, \Sigma$, and Ξ) where the interactions are among the same kinds baryons through meson exchanges. $\mathcal{L}_{BM}$ can be expressed as

$$\mathcal{L}_{BM} = \sum_B \overline{\Psi}_B \Big[i\gamma^\alpha \partial_\alpha - (m_B - g_{\sigma B}\sigma) - \Big(g_{\omega B}\gamma^\alpha \omega_\alpha + \frac{1}{2} g_{\rho B}\gamma^\alpha \tau_B \cdot \rho_\alpha + g_{\phi Y}\gamma^\alpha \phi_\alpha \Big) \Big] \Psi, \tag{3}$$

with m_B the baryon mass. The coupling constants of the nonstrange mesons coupled to all baryons are denoted by $g_{\sigma B}$, $g_{\omega B}$, and $g_{\rho B}$. $g_{\phi Y}$ are the coupling constants of the hidden-strangeness meson coupled with hyperons ($Y = \Lambda, \Sigma$, and Ξ). $\mathcal{L}_M$ is the Lagrangian density for free and self-interaction mesons. $\mathcal{L}_M$ takes following form:

$$\mathcal{L}_M = \tfrac{1}{2}\big(\partial_\alpha \sigma \partial^\alpha \sigma - m_\sigma^2 \sigma^2\big) + \tfrac{1}{2}\big(\partial_\alpha \sigma^* \partial^\alpha \sigma^* - m_{\sigma^*}^2 \sigma^{*2}\big) - \tfrac{1}{4}\omega_{\alpha\beta}\omega^{\alpha\beta} + \tfrac{1}{2} m_\omega^2 \omega_\alpha \omega^\alpha - \tfrac{1}{4}\phi_{\alpha\beta}\phi^{\alpha\beta} + \tfrac{1}{2} m_\phi^2 \phi_\alpha \phi^\alpha - \tfrac{1}{4}\rho_{\alpha\beta}\cdot\rho^{\alpha\beta} + \tfrac{1}{2} m_\rho^2 \rho_\alpha \cdot \rho^\alpha, \tag{4}$$

where the $\omega^{\alpha\beta}$, $\phi^{\alpha\beta}$, and $\rho^{\alpha\beta}$ are meson tensor fields of the ω, ϕ, and ρ mesons, respectively. Their explicit forms are $\omega^{\alpha\beta} = \partial^\alpha \omega^\beta - \partial^\beta \omega^\alpha$, $\phi^{\alpha\beta} = \partial^\alpha \phi^\beta - \partial^\beta \phi^\alpha$, and $\rho^{\alpha\beta} = \partial^\alpha \rho^\beta - \partial^\beta \rho^\alpha$, respectively. $\mathcal{L}_M^{\rm NL}$ is the Lagrangian density for describing the nonlinear and cross self-interactions among σ, ω, and ρ mesons. $\mathcal{L}_M^{\rm NL}$ can be expressed as

$$\begin{aligned}\mathcal{L}_M^{\rm NL} = &-\frac{\kappa_3 g_{\sigma N} m_\sigma^2}{3! m_N}\sigma^3 - \frac{\kappa_4 g_{\sigma N}^2 m_\sigma^2}{4! m_N^2}\sigma^4 + \frac{\zeta_0 g_{\omega N}^2}{4!}(\omega_\alpha \omega^\alpha)^2 \\ &+ \frac{\eta_1 g_{\sigma N} m_\omega^2}{2! m_N}\sigma \omega_\alpha \omega^\alpha + \frac{\eta_2 g_{\sigma N}^2 m_\omega^2}{4 m_N^2}\sigma^2 \omega_\alpha \omega^\alpha \\ &+ \frac{\eta_\rho g_{\sigma N} m_\rho^2}{2! m_N}\sigma \rho_\alpha \cdot \rho^\alpha + \frac{\eta_{1\rho} g_{\sigma N}^2 m_\rho^2}{4 m_N^2}\sigma^2 \rho_\alpha \cdot \rho^\alpha \\ &+ \frac{\eta_{2\rho} g_{\omega N}^2 m_\rho^2}{4 m_N^2}\omega_\alpha \omega^\alpha \rho_\alpha \cdot \rho^\alpha.\end{aligned} \tag{5}$$

Note that in the nucleon sector of RMF models, the values of baryon-meson couplings and other free parameters are relatively certain because they are obtained by fitting the model to the observables of finite nuclei and nuclear matter. The obtained coupling constants and parameter values depend on the chosen observables and their corresponding weights. The exact values of the corresponding parameters of the RMF parameter sets used in this work can be seen in Refs.[64,69,108,110,111]. Here we will calculate some nuclear matter properties predicted by selected RMF parameter sets, i.e., BSP [64,109], G3 [108], TM1e [110], FSUGarnet [111], and FSU2H [69]. The results are shown in Table I, Fig. 2, and Fig. 3 and the results are compared to experimental data and other calculations. In Table I, we show the energy expansion parameters of nuclear matter predicted by those parameter sets. There are isoscalar parameters, isovector parameters, and core-crust transition properties. The isoscalar parameters at saturation density are K_0 and Q_0. K_0 and Q_0 as the second and third derivatives of binding energy $E(\rho)$, respectively. They are defined as [137]

$$\begin{aligned} K_0 &= 9\rho_0^2 \frac{d^2 E(\rho)}{d\rho^2}\bigg|_{\rho=\rho_0}, \\ Q_0 &= 27\rho_0^3 \frac{d^3 E(\rho)}{d\rho^3}\bigg|_{\rho=\rho_0}. \end{aligned} \tag{6}$$

The isovector parameters at saturation density are L and $K_{\rm sym}$. L and $K_{\rm sym}$ are first and second derivatives of the symmetry energy $E_{\rm sym}$, respectively. They are defined as [137]

$$\begin{aligned} L &= 3\rho_0 \frac{dE_{\rm sym}}{d\rho}\bigg|_{\rho=\rho_0}, \\ K_{\rm sym} &= 9\rho_0^2 \frac{d^2 E_{\rm sym}}{d\rho^2}\bigg|_{\rho=\rho_0}. \end{aligned} \tag{7}$$

The core-crust transition density and pressure ρ_t and P_t are calculated using a relativistic random phase approximation [138,139]. They play a primary role in determining the NS's core-crust properties. The ρ_t and P_t are sensitive to the slope of symmetry energy L. ρ_t and P_t also have a relation with other

TABLE I. The nuclear matter parameters at the saturation density ρ_0 and the core-crust transition properties predicted by BSP [64,109], G3 [108], TM1e [110], FSUGarnet [111], and FSU2H [69] parameter sets, respectively. All quantities of nuclear matter parameters are given in MeV units, except the units for ρ_t and P_t are fm^{-3} and $\mathrm{MeV/fm}^{-3}$, respectively.

	BSP	G3	TM1e	FSUGarnet	FSU2H	Constraints	Refs.
E/N	−16.0	−15.7	−16.23	−16.26	−16.29	-15.9 ± 0.4	[140]
K_0	241.61	257	309.89	231.64	248.78	230 ± 40	[141]
E_{sym}	29.3	30.71	32.13	30.94	30.44	31.7 ± 3.2	[142–144]
L	51.5	45.69	42.46	51.05	42.6	58.7 ± 28.1	[142–144]
Q_0	−338.62	−494.45	−295.81	15.18	31.18	$-800 \leqslant Q_0 \leqslant 400$	[145–147]
K_{sym}	10.67	−95.96	−235.94	−246.648	129.194	$-400 \leqslant K_{\mathrm{sym}} \leqslant 100$	[145–147]
P_t	0.29	0.566	0.298	0.244	0.055	0.339 ± 0.115	[148]
ρ_t	0.087	0.090	0.092	0.083	0.089	0.072 ± 0.011	[148]

nuclear matter parameters. A discussion of the correlation between ρ_t and P_t with nuclear matter parameters can be found in, for example, Ref. [45].

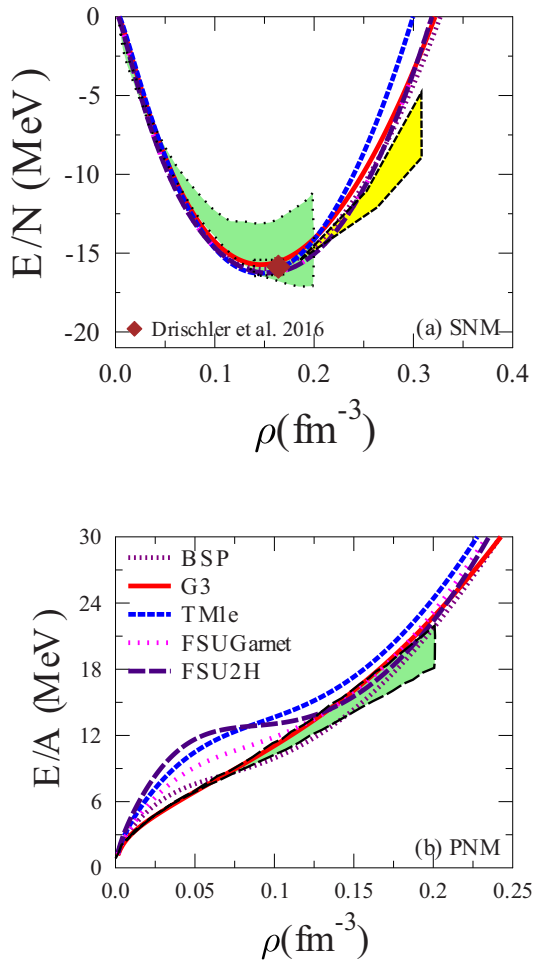

FIG. 2. The binding energy of pure neutron matter (PNM) and symmetric nuclear matter (SNM) predictions from the used RMF parameter sets. RMF results are compared to existing experimental data and the chiral effective field calculation result. The shaded areas are a result of chiral effective field calculations [149] and fractional order proportional and integral (FOPI) experimental data [150] shown in the light green and yellow colors, respectively.

For the SNM case, it is evident that all parameter sets are compatible with the chiral effective field calculations [149]. For the region near the saturation density, the binding energy results are shown in panel (a) of Fig. 2 and the EOS is shown in panel (a) of Fig. 3. It can also be observed that the pressure profiles of the SNM EOS for all parameter sets are compatible with the one from FOPI experimental data [150] in the low-density region and the one from heavy-ion experimental data [151] in the moderate-density region, as shown in panel (b) of Fig. 3. The one predicted by the TM1e parameter set at moderate density is stiffer than those of the other parameter sets. For the PNM case, only the binding energies and EOSs predicted by G3 and BSP parameter sets are compatible with chiral effective field calculations [149] for all regions. For the region near the saturation density, the binding energy results are shown in panel (b) of Fig. 2 whereas the EOS is shown in panel (a) of Fig. 3. The pressure profiles predicted by all parameter sets are compatible with chiral effective field calculations [104] as shown in panel (c) of Fig. 3. Moreover, it can be seen in panel (c) of Fig. 3 that the pressure profiles predicted by all parameter sets are compatible with the ones deduced from heavy-ion experimental data [151] at moderate density. However, the EOS predicted by the G3 parameter set tends to be softer than those of other parameter sets.

In panel (a) of Fig. 4, we compare the NS EOSs predicted by those parameter sets without considering hyperons with several observation constraints. In panel (a) of Fig. 4, it is shown that the ones of FSU2H and TM1e are relatively compatible with an upper limit results obtained using the nonparametric analysis of Landry *et al.* [43] at $P(\rho_0)$ while the ones of G3 and BSP are compatible with all constraints used at $P(2\rho_0)$. Moreover, at $P(6\rho_0)$, the results of all parameter sets used are compatible with the one of nonparametric analysis of Landry *et al.* [43]. At $P(\rho > 2\rho_0)$, the EOS predicted by FSU2H tends to be stiffer than those of other parameter sets. Also, in panel (a) of Fig. 4 it can be observed that the EOS results of G3 and BSP parameter sets are relatively stiff while the ones of TM1e and FSUGarnet parameter sets are soft at $P(\rho > 3\rho_0)$. Generally, The EOSs of all parameter sets used are quite compatible with data taken from multimessenger observations analysis [1,36,43,44].

It can be seen in Table I that, compared to that of BSP, the core-crust transition pressure of G3 is not too compatible with the one from the recent constraint. The reason is the role of

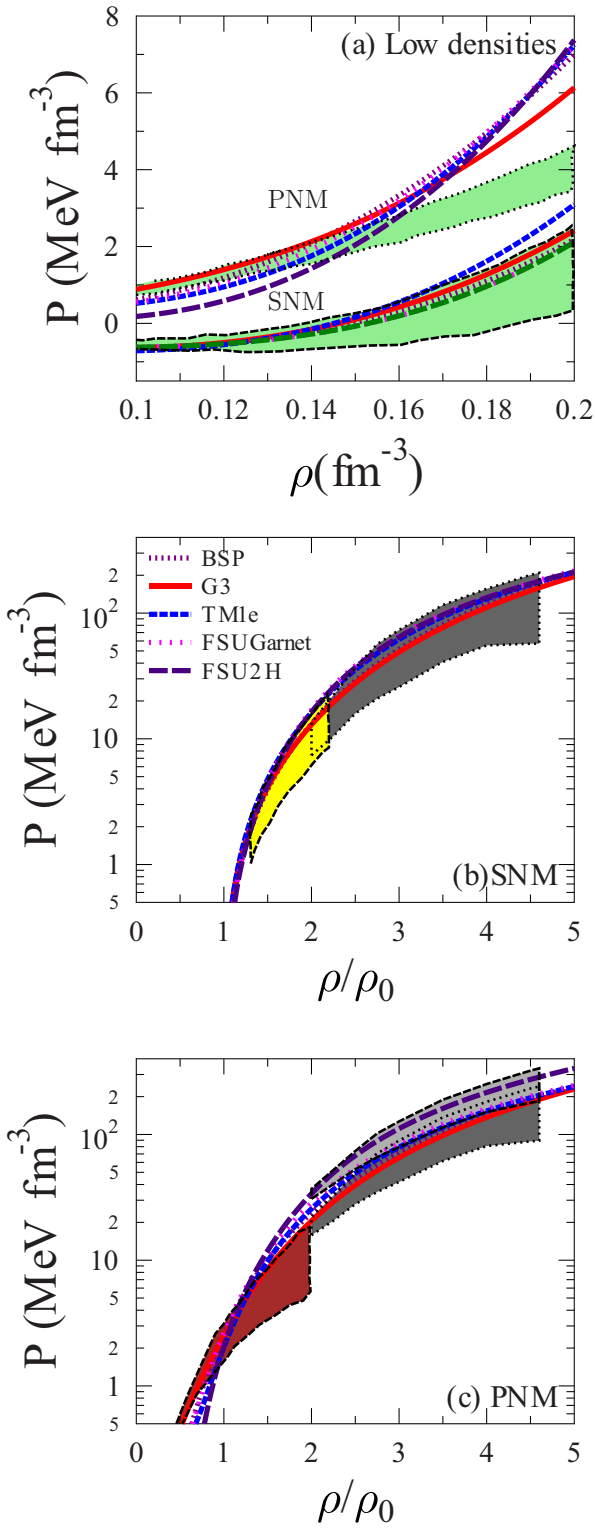

FIG. 3. (a) Pressure as a function of the density around the saturation density for PNM and SNM predicted by the used RMF parameter sets. (b) for SNM and (c) for PNM. The light green shaded regions in the top panel result from chiral effective field calculations in Ref. [149]. The gray-shaded areas in (b) and (c) show the ones from heavy-ion experimental data [151]. The brown shaded regions in the bottom panel are the ones from chiral effective field calculations in Ref. [104].

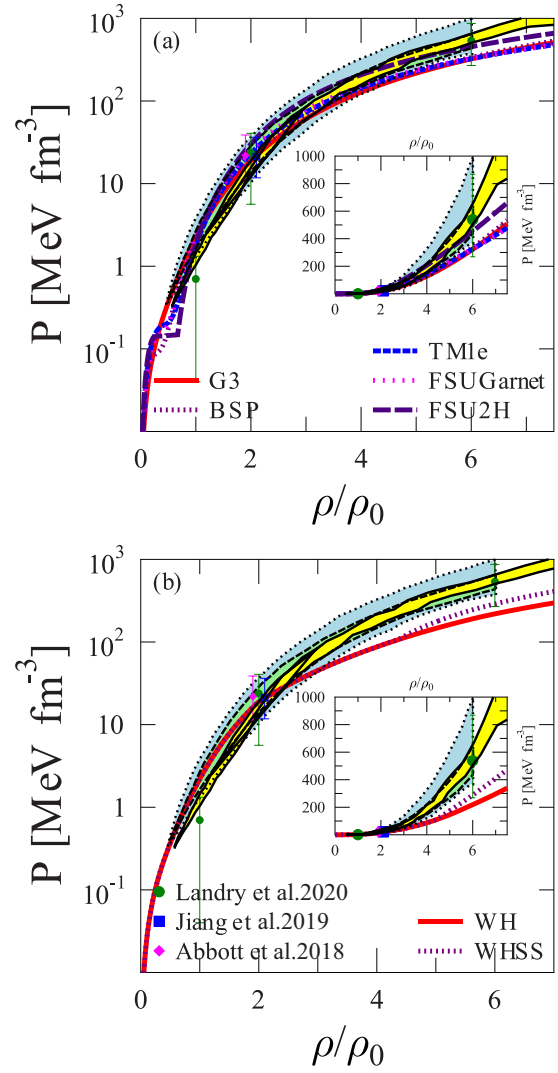

FIG. 4. (a) Pressure as a function of density around the saturation density for NS without hyperons predicted using the selected RMF parameter sets used in this work. Panel (b) is similar to (a) but with hyperons included and only for the G3 parameter set. Here, we consider two cases, WHSS and WH. The results are compared to the existing GW observation and Bayesian results. In both panels, we insert three pressure and various density constraints for comparison. Those are the ones from GW170817 [1,36], one from nonparametric analysis using recent observation of a gravitational wave and pulsar [43], and the one joint analysis of NICER, the nuclear data, and GW170817 [44].

δ meson in the G3 parameter set, where this meson softens the symmetry energy at subsaturation densities and stiffens the EOS at high densities [108,152,153]. Consequently, the presence of δ mesons can affect the maximum mass of NSs and other properties of highly asymmetric nuclear systems [108]. Although G3 does not fulfill the constraint of the transition pressure, The binding energy and the pressure of the PNM EOS of G3 are consistent with chiral effective field calculations [104,149] as shown in panel (b) of Fig. 2 and in panels (a) and (c) of Fig. 4. Recent discussions of the progress and state of the art of chiral many-body perturbation

theory (MBPT) results can be found in Refs. [154,155]. It is noteworthy that, recently, the PREX-II experiment reported a new result on the neutron skin thickness of ^{208}Pb, $R_{\rm skin}^{208} = 0.29 \pm 0.07$ fm, which is relatively larger than other existing $R_{\rm skin}^{208}$ experimental results. The Ref. [41] authors deduced from this result a relatively high $L = 110 \pm 34$ MeV. A recent study [46] has shown that astrophysical constraints on L and $R_{\rm skin}^{208}$ using combined astrophysical data with PREX-II and chiral effective field theory constraints are $L = 58 \pm 19$ MeV and $R_{\rm skin}^{208} = 0.19^{+0.03}_{-0.04}$ fm, respectively. The Ref. [46] authors concluded that extrapolating neutron skin thickness to NS scale requires a careful treatment of systematic EOS model uncertainties. In particular, the PREX-II results do not require large NS radii. However, if the high L value of PREX-II persists, it can mean a peak in the speed of sound around saturation density. This $R_{\rm skin}^{208}$ value issue is important for our understanding of nuclear matter; however, in this work, we do not want to discuss this matter deeper. To this end, in general, we can conclude that the nuclear matter and NS matter results predicted by the used RMF parameter sets are compatible with experimental data and other calculations. However, the G3 parameter provides a better result than those of others selected RMF parameter sets studied in this work.

Hyperons and other exotic particle coupling constants in the matter are experimentally difficult to constrain. Consequently, the contribution in the EOS from the hyperon sector is uncertain. The hyperon contribution in the EOS appears at high densities—when hyperons contribution is considered in the EOS—and the predicted maximum mass is smaller than the predicted maximum mass without hyperons. This is evidence because the hyperons being more massive than nucleons makes the EOS softer. In the current work, we only include hyperons but neglect other exotic particles. We use the recent SU(3) prescription [62,63,69] and an experimental value of potential depths at nuclear matter saturation density [130] to determine hyperon coupling constants. Note that the NS EOS based on SU(3) in the hyperon sector is slightly stiffer than that based on standard SU(6). The hyperon vector-coupling constants based on SU(3) symmetry can be expressed as

$$\begin{aligned} g_{\omega N} : g_{\omega\Lambda} : g_{\omega\Sigma} : g_{\omega\Xi} &= 3 : 2 : 2 : 1, \\ g_{\rho N} : g_{\rho\Lambda} : g_{\rho\Sigma} : g_{\rho\Xi} &= 1 : 0 : 1 : 1, \\ g_{\omega N} : g_{\phi\Lambda} : g_{\phi\Sigma} : g_{\phi\Xi} &= 3 : -\sqrt{2} : -\sqrt{2} : -2\sqrt{2}, \\ g_{\phi N} &= 0. \end{aligned} \tag{8}$$

We obtain the hyperon scalar coupling constants $g_{\sigma Y}$ from the potential depths of hyperons of the symmetric nuclear matter saturation density ρ_0. The potential depths of hyperons Y are

$$U_Y^{(N)}(\rho_0) = g_{\omega Y}\omega(\rho_0) - g_{\sigma Y}\sigma(\rho_0). \tag{9}$$

In this work, the experimental values of the potential depth of hyperons at saturation density are given by [156]

$$\begin{aligned} U_\Lambda^{(N)} &= -28 \text{ MeV}, \quad U_\Sigma^{(N)} = +30 \text{ MeV}, \\ \text{and } U_\Xi^{(N)} &= -18 \text{ MeV}. \end{aligned} \tag{10}$$

In panel (b) of Fig. 4, we show the impact of hyperons on the NS EOS predicted by the G3 parameter set. Generally, the role of hyperons softens the EOS at high densities. The recent EOS constraints are more compatible with the NS EOS without hyperons than those with hyperons. However, for the EOS with hyperons included and using the $v_s^{\max} = \frac{1}{\sqrt{3}}$ constraint at high densities, the corresponding EOS can be slightly increased, though the corresponding stiffening impact is not too significant. This effect is insufficient to push the EOS at high densities closer to the EOS constraint from the GW170817 event.

III. ANISOTROPIC NEUTRON STARS PROPERTIES

In this section, we briefly discuss the anisotropic pressure models and NS properties such as mass-radius relations, tidal deformability, and the moment of inertia.

The local anisotropic pressure correction emerges in the Tolman-Oppenheimer-Volkoff (TOV) equation if the radial pressure is assumed not to be identical with the tangential pressure. This correction provides an additional force in the TOV equation through the nonzero value of the difference between the radial and tangential pressures. The pressure difference denoted by σ plays two roles. The sign of σ determines the direction of the force. The direction can be outward from or inward to the star's center. The function of σ determines the strength and distribution of the force [76]. In this work, we use three anisotropic pressure models. The models are constructed using (i) Bowers and Liang, denoted by $\sigma_{\rm BL}$ [112], (ii) Horvat *et al.*, denoted by $\sigma_{\rm DY}$ [51], and (iii) Cosenza *et al.*, denoted by $\sigma_{\rm HB}$ [113]. The explicit forms of the corresponding anisotropic models [51,112,113,157,158] are

$$\begin{aligned} \sigma_{\rm BL} &\equiv -\frac{\eta(\epsilon + 3P)(\epsilon + P)r^2}{3\left(1 - \frac{2M}{r}\right)}, \\ \sigma_{\rm DY} &\equiv \frac{2MP\Delta}{r}, \\ \sigma_{\rm HB} &\equiv -\frac{r(1-\zeta)}{2\zeta}\frac{dP}{dr}, \end{aligned} \tag{11}$$

respectively. η, Δ, and ζ are free parameters for each model. The free parameters give the strength for each model. Note that $\sigma \equiv P - Q$. P and Q are the radial and tangential pressure, respectively.

The $\sigma_{\rm BL}$ model is constructed to be gravity-induced anisotropic pressure. Consequently, the $\sigma_{\rm BL}$ depends nonlinearly on the radial pressure and energy density [112]. $\sigma_{\rm BL}$ vanishes at the center to yield regular solutions. The $\sigma_{\rm DY}$ model is based on a quasilocal ansatz. This model is linear in P and continuous at the surface of the star [51]. Note that in the DY model the fluid becomes isotropic at the center. Therefore, this model is important only for relativistic configurations, which agree that anisotropy can arise at high densities. Furthermore, it is common to assume that $-2 \leqslant \Delta \leqslant 2$ in many studies. (Please see Refs. [74,85] and the references therein.) Differing from $\sigma_{\rm BL}$ and $\sigma_{\rm DY}$ models, the $\sigma_{\rm HB}$ model is constructed using a heuristic procedure. Like other models, this model also guarantees that anisotropy must vanish at the center [74]. Detailed discussions of this model can be found in Ref. [113]. Note that anisotropy affects the stellar instability and the critical central density where

$dM/d\rho_c = 0$ does not always correspond to the onset of instability. For $\sigma_{\rm BL}$ and $\sigma_{\rm HB}$ models, the maximum point of $M(\rho_c)$ does not indicate the onset of instability due to radial pulsation [74]. Another instability that can occur only in an anisotropic fluid is cracking or overturning. These instabilities (cracking or overturning) occur because of a tendency of the self-gravitating body to split or compress after its equilibrium state is disturbed. Please see examples Refs. [77–80,89] for details. It is reported in Ref. [77] that if the $\sigma_{\rm DY}$ model has a negative value of Δ and the $\sigma_{\rm HB}$ model has ζ value less than 1, the stars are stable to cracking. Furthermore, it is also shown [76,77] that the $\sigma_{\rm DY}$, $\sigma_{\rm HB}$, and $\sigma_{\rm BL}$ models in the parameter value range investigated satisfy all energy conditions of a perfect fluid.

We start the NS properties discussion from the stress-energy tensor with anisotropic pressure [157,158]:

$$T_{\alpha\beta} = \epsilon u_\alpha u_\beta + P k_\alpha k_\beta + Q[g_{\alpha\beta} + u_\alpha u_\beta - k_\alpha k_\beta], \tag{12}$$

where $g_{\alpha\beta}$ is the space-time metric, u_α is the fluid 4-velocity, and ϵ is the total energy density. $u^\alpha k_\alpha$=0 because k_α is the unit radial vector orthogonal to u^α. Note that $g_{\alpha\beta} + u_\alpha u_\beta - k_\alpha k_\beta$ is the projection tensor onto the 2-surface orthogonal to k_α and u_α. We use the standard static spherical symmetric line element to define the space-time metric. The metric can be written as

$$ds_0^2 = -e^{2\nu}dt^2 + e^{2\lambda}dr^2 + r^2(d\theta^2 + \sin^2\theta\, d\phi^2). \tag{13}$$

We insert Eq. (13) into Einstein field equations,

$$G^\alpha_\beta = 8\pi T^\alpha_\beta; \tag{14}$$

then we can obtain the anisotropic TOV equation as follows:

$$\begin{aligned}
\frac{dM}{dr} &= 4\pi\epsilon r^2, \\
\frac{dP}{dr} &= -(\epsilon + P)\frac{d\nu}{dr} - \frac{2\sigma}{r}, \\
\frac{d\nu}{dr} &= \frac{M + 4\pi r^3 P}{r(r - 2M)}.
\end{aligned} \tag{15}$$

If we set σ =0, the anisotropic TOV equation reduces to the isotropic TOV equation. An NS can deform when another NS approaches it. The approaching NS provides an external gravitational tidal field ($\mathcal{E}_{ij}$) on the corresponding NS, and the response of the corresponding NS emerges as the NS quadrupole moment (Q_{ij}). Therefore, the NS quadrupole moment has a linear relation with the external tidal field as [159]

$$Q_{ij} = -\lambda\mathcal{E}_{ij}, \tag{16}$$

where λ is the tidal deformability parameter. λ can be expressed as

$$\lambda = \tfrac{2}{3}k_2 R^5, \tag{17}$$

where k_2 is the electric-tidal Love number. The tidal deformability parameter can be expressed as a dimensionless quantity. The dimensionless tidal deformability can be expressed as [160]

$$\Lambda = \frac{2k_2}{3C^5}, \tag{18}$$

where $C = \frac{2M(R)}{R}$ is the compactness of NS, while $M(R)$ and R are the NS mass and radius, respectively. The dimensionless tidal deformability is a crucial property in which can be extracted from GW events.

To calculate tidal deformability, we start from the perturbed nonrotating line element to calculate k_2. The corresponding line element can be expressed as [161]

$$ds^2 = ds_0^2 + ds_1^2. \tag{19}$$

ds_0^2 is the same as in Eq. (13). ds_1^2 can be expressed as

$$\begin{aligned}
ds_1^2 = &-e^{2\nu}H(r)Y_{20}(\theta,\phi)dt^2 + e^{2\lambda}H(r)Y_{20}(\theta,\phi)dr^2 \\
&+ r^2K(r)Y_{20}(\theta,\phi)d\theta^2 + r^2\sin^2\theta K(r)Y_{20}(\theta,\phi)d\phi^2,
\end{aligned} \tag{20}$$

where $Y_{20}(\theta,\phi)$ is spherical harmonic function with $l = 2$ and $m = 0$. We insert Eq. (20) into perturbed Einstein field equations:

$$\delta G^\alpha_\beta = 8\pi\delta T^\alpha_\beta \tag{21}$$

The perturbed stress-energy tensor shown on the right-hand side of Eq. (21) has the following relations: $\delta T^t_t = -\delta\epsilon = -\frac{d\epsilon}{dP}\delta P$, $\delta T^r_r = \delta P$, and $\delta T^\theta_\theta = \delta T^\phi_\phi = \delta Q = (1 - \frac{d\sigma}{dP})\delta P$. By following Eq. (21), we obtain the relation between $K(r)$ and $H(r)$ from $\delta G^r_\theta = 0$ that can be written as

$$\frac{dK}{dr} = -\frac{dH}{dr} - H\frac{d\nu}{dr}, \tag{22}$$

$$\frac{d^2K}{dr^2} = -\frac{d^2H}{dr^2} - \frac{dH}{dr}\frac{d\nu}{dr} - H\frac{d^2\nu}{dr^2}. \tag{23}$$

We insert Eqs. (22) and (23) into $\delta G^t_t - \delta G^r_r = 8\pi(\delta T^t_t - \delta T^r_r)$ and then we obtain a second-order differential equation that can be written as

$$\frac{d^2H}{dr^2} + A_1\frac{dH}{dr} + A_2H = 0, \tag{24}$$

where

$$A_1 = \frac{2}{r} + e^{2\lambda}\left(\frac{2M}{r^2} + 4\pi r(P - \epsilon)\right), \tag{25}$$

$$\begin{aligned}
A_2 = e^{2\lambda}&\left(-\frac{6}{r^2} + \frac{4\pi(P+\epsilon)\left(1 + \frac{d\epsilon}{dP}\right)}{1 - \frac{d\sigma}{dP}} + 4\pi(4\epsilon + 8P)\right) \\
&+ 16\pi\sigma e^{2\lambda} - \left(\frac{d\nu}{dr}\right)^2.
\end{aligned} \tag{26}$$

Our result is the same as presented in Ref. [162] However, our result slightly differs from Ref. [84]. In Ref. [84], there is no $16\pi\sigma e^{2\lambda}$ term. If we set $y \equiv \frac{rH'}{H}$, then Eq. (24) turns into a first-order differential equation that can be written as

$$r\frac{dy}{dr} + y^2 + A_3y + A_4r^2 = 0, \tag{27}$$

where

$$A_3 = \frac{r - 4\pi r^3(\epsilon - P)}{r - 2M}, \tag{28}$$

$$A_4 = \frac{4\pi r\left(4\epsilon + 8P + \frac{(\epsilon+P)\left(1+\frac{d\epsilon}{dP}\right)}{1-\frac{d\sigma}{dP}} + 4\sigma\right)}{r - 2M} - 4\left(\frac{M + 4\pi r^3 P}{r^2\left(1 - \frac{2M}{r}\right)}\right)^2. \tag{29}$$

We set $y(0)$ as the initial value of y to numerically solve Eq. (27) and the TOV equation simultaneously using the Runge-Kutta method. Next, we can calculate k_2 by using the expression in Eq. (30):

$$k_2 = \frac{A_5}{A_6}, \tag{30}$$

where

$$A_5 = \tfrac{8}{5}(1 - 2C)^2 C^5[2C(Y - 1) - Y + 2], \tag{31}$$

$$A_6 = 2C[4(Y + 1)C^4 + (6Y - 4)C^3] + 2C[(26 - 22Y)C^2 + 3(5Y - 8)C - 3Y + 6] - 3(1 - 2C)^2[2C(Y - 1) - Y + 2]\ln\left(\frac{1}{1 - 2C}\right), \tag{32}$$

Note that $Y = y(R)$. After we obtain k_2, we can calculate Λ that can be compared with data from GW observations.

To calculate NS moment of inertia, we start from the approximate line element for a slowly rotating star in which can be written as

$$ds^2 = ds_0^2 + ds_2^2. \tag{33}$$

ds_0^2 is the same with Eq. (13). However, ds_2^2 can be expressed as [163]

$$ds_2^2 = -2\omega(r)r^2 \sin^2\theta\, dt\, d\phi. \tag{34}$$

The frame-dragging effect is considered through $\omega(r)$. In the current work, we use a slowly rotating approximation. Herein, slowly rotating means that the angular velocity of a uniform rotating NS (Ω) is much less than the Kepler angular velocity (Ω_K). There are two methods to calculate the moment of inertia of an NS, i.e., the integration method and solving the second-order differential method. For this work, we choose to solve the second-order differential equation, where the corresponding differential equation is obtained from Eq. (34) and the final form can be expressed as [82]

$$\frac{1}{r^4}\frac{d}{dr}(r^4 J\bar{\omega}) + \frac{4}{r^4}\frac{dJ}{dr}\left(1 + \frac{\sigma}{\epsilon + P}\right)\bar{\omega} = 0, \tag{35}$$

where the anisotropic correction enters the second term. Here,

$$J \equiv e^{-\nu}\left(1 - \frac{2M}{r}\right)^{1/2}, \tag{36}$$

$$\bar{\omega}(r) \equiv \Omega - \omega(r). \tag{37}$$

Equation (35) can be factorized into two first-order differential equations as

$$\frac{d\tilde{\omega}}{dr} = \frac{6}{r^4}e^{\nu}\left(1 - \frac{2M}{r}\right)^{-1/2}\tilde{\kappa},$$

$$\frac{d\tilde{\kappa}}{dr} = \frac{8\pi}{3}\frac{r^4 e^{-\nu}(\epsilon + P)}{(1 - \frac{2M}{r})^{1/2}}\left(1 + \frac{\sigma}{\epsilon + P}\right)\tilde{\omega}. \tag{38}$$

Equation (38) can be solved using the Rungge-Kutta method with boundary conditions:

$$\tilde{\omega}(R) = 1 - \frac{2I}{R^3},$$

$$\tilde{\kappa}(R) = I, \tag{39}$$

where I in Eq. (39) is the NS moment of inertia.

IV. RESULTS AND DISCUSSIONS

This section discusses the anisotropic NS property predictions. The results are compared with the constraints extracted from observation data. First, we examine the impact of the corresponding EOS on the mass and radius of the NS, as shown in Fig 5. The DY and HB models predicted that the NS maximum mass increases by decreasing the value of the free anisotropic parameter. However, the increasing mass is always followed by significant increase of the corresponding radius. For isotropic and anisotropic NSs, the impact of the conformal bound of the speed of sound at high densities (WHSS) appears in the form of increasing the maximum mass value. However, for an anisotropic NS, if we adjust the corresponding anisotropic parameter appropriately, the maximum mass predicted by both EOSs with and without considering the conformal bound of the speed of sound at high densities is the same. Moreover, WHSS provides smaller relative radii predictions than those without this requirement WH.

It is evident that the radius range constraints of a $1.4M_\odot$ NS by Refs. [41,43] and the recent range of maximum mass $M_{\rm TOV}$ from Refs. [49] can be fulfilled simultaneously by all anisotropic models by adjusting their free anisotropic parameters for WHSS and WH EOSs. These results can be seen in Fig. 5, for cases with $\eta = 2.65$, $\Delta = -1.8$, and $\zeta = 0.71$ for the WH EOS and for cases with $\eta = 1.85$, $\Delta = -1.16$, and $\zeta = 0.79$ for the WHSS EOS, respectively. However, only the DY (WH and WHSS) and BL WHSS anisotropic models show radii results that also are compatible simultaneously with the narrow range radius constraint of a $1.4M_\odot$ NS predicted by the NICER Collaboration [33,34]. Moreover, if we also include the radius constraint of a $2.08M_\odot$ NS predicted by the NICER Collaboration [33,34], then only DY WH is compatible with all the above constraints [33,34,41,43,49]. Furthermore, if we also use a narrower range of the $1.4M_\odot$ NS radius constraint than the one of NICER, i.e., the one of Breschi *et al.* [42], then we have found that only DY WHSS with $\Delta = -1.16$ is fully compatible with this constraint. From another view, this EOS is already outside the radius constraint range of a $2.08M_\odot$ NS predicted by the NICER Collaboration [33,34], whereas the one of DY WH with $\Delta = -1.8$, which is compatible with the $2.08M_\odot$ NS constraint by NICER, provides a $1.4M_\odot$ NS

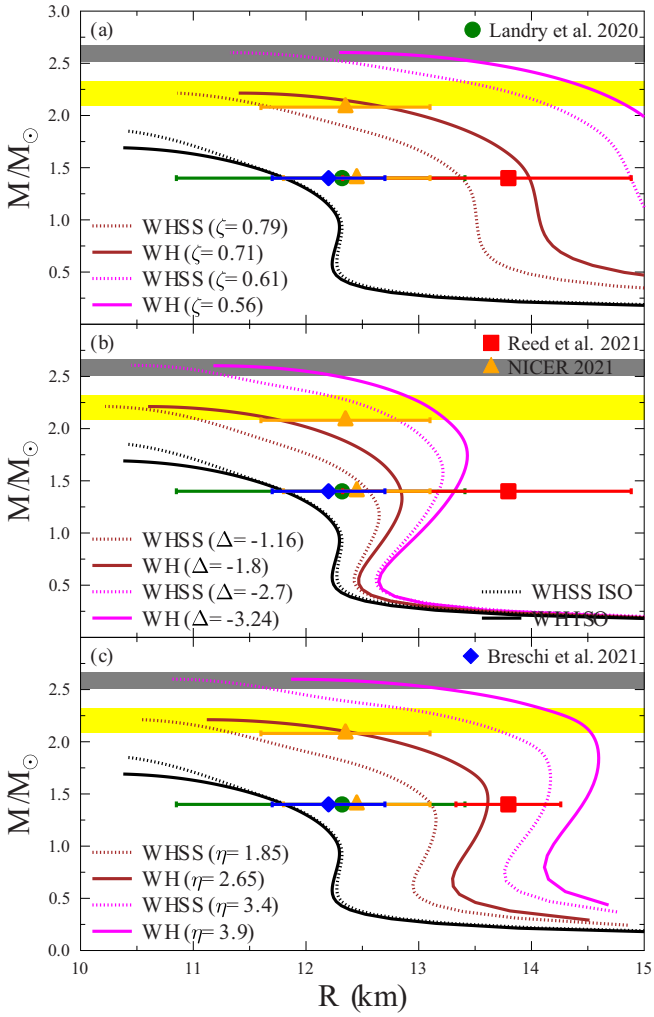

FIG. 5. Mass-radius relation of an NS with anisotropic pressure including the hyperon contribution and the speed of sound treatment. We show the impact of the free anisotropic variation of the $\sigma_{\rm BL}$ model in panel (a), the one of the $\sigma_{\rm DY}$ model in panel (b), and the one of the $\sigma_{\rm HB}$ model in panel (c). We include small and large radii constraints. Small radii constraints are taken from Refs. [42,43] while the large one is from Ref. [41]. We also include radius constraints from NICER 2021 [33,34]. The shaded areas are the range of maximum mass from Ref. [49] and the range of the secondary object mass of the GW190814 event [1], shown by yellow and gray colors, respectively.

radius that is slightly larger but close to the upper bound of the radius constraint from Breschi *et al.*. We note that compared to one of our previous reports [82], the obtained parameter value of the DY WH EOS that is most compatible with all constraints, including the one from Breschi *et al.* [42], i.e., $\Delta = -1.8$ is slightly larger. All constraints used to prefer an EOS within the DY model with the conformal bound at high densities are violated.

To check whether or not the $2.6M_\odot$ mass from the secondary object from the GW190814 event [1] is an anisotropic NS, we increase the maximum mass constraint to $2.6M_\odot$, as shown in the gray band in Fig. 5. The $1.4M_\odot$ NS radius range constraints [33,34,41,43] and the one for a $2.08M_\odot$ NS reported by the NICER Collaboration [33,34], and the $2.6M_\odot$ mass from the secondary object from the GW190814 event [1], can only be fulfilled simultaneously by the mass-radius relation predicted by the DY model using the WHSS EOS with $\Delta = -2.7$. However, if we consider that the DY parameter range is $-2 \leqslant \Delta \leqslant 2$, as used in the literature [74,85], then $\Delta = -2.7$ is less than the lower bound of this range. The DY model with the WH EOS with $\Delta = -3.24$ is not compatible with the radii constraints for $2.08M_\odot$ and $1.4M_\odot$ NSs reported by the NICER Collaboration [33,34]. To this end, we also should emphasize that none of the corresponding anisotropic models studied in this work are compatible with the combined constraints from Breschi *et al.* [42] and $2.6M_\odot$, respectively. It is interesting to check if we can neglect the small $1.4M_\odot$ NS radius constraint from Refs. [33,34,42,43] and the radius constraint for a $2.08M_\odot$ NS reported by the NICER Collaboration [33,34]. Therefore, we only consider the relatively larger radius constraint of Reed *et al.* [41]. We have found that mass-radius results of the anisotropic models considered in this work such as the BL model WHSS with $\eta = 2.65$, DY models WH and WHSS with $\Delta = -2.7$ and $\Delta = -3.34$, and the HB model WHSS using $\zeta = 0.61$ are relatively compatible with both constraints from Refs. [1,41], respectively. It means the role of the small $1.4M_\odot$ NS radius constraints from Refs. [33,34,42,43] and the radius constraint for a $2.08M_\odot$ NS reported by the NICER Collaboration [33,34] are crucial for determining whether or not the $2.6M_\odot$ mass from the secondary object from the GW190814 event [1] is an anisotropic NS. To this end, it is evident from these results that the mass-radius result predicted by the DY anisotropic model, in general, is more compatible with the used NS maximum mass and radius constraints [33,34,41–43,49] in this work. The compatibility of the DY model results with the recent constraints compared to other anisotropic models is due to the predicted compactness of NSs within the DY model being sensitive to the variation of the free parameter of the DY anisotropic model. The impact of the anisotropic parameter variation Δ of the DY model on NS compactness is shown in Fig. 6. Note that increasing the absolute value Δ from zero significantly increases the compactness. Even the corresponding compactness can get through the NS compactness constraint of Refs. [28,164] and the highest compactness of NSs reported in Ref. [165] for the case of WHSS with $M > 2.6M_\odot$. Additionally, note that the conformal bound on the speed of sound makes NSs more compact. However, recent constraints used in this work favor the conformal bound being violated in an anisotropic NS with hyperons. A compact object with a mass around $2.6M_\odot$ and observed as the secondary object from the GW190814 event is unlikely an anisotropic NS.

For completeness, we will also study the tidal deformability and the moment of inertia of NSs predicted by the DY anisotropic model, as shown in Fig. 7. The results are also compared to the analysis of the observations data of Refs. [36,41,43]. In panel (a) in Fig. 7, we can observe that the impact of anisotropic pressure with Δ and EOS variations on k_2 starts appearing for NS masses larger than half of the solar mass, and this effect becomes significant for larger NS masses. The k_2 peak yielded by an anisotropic NS is relatively

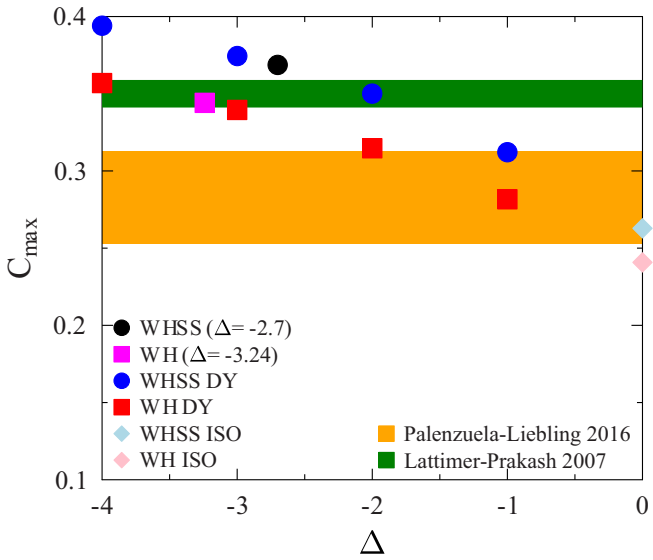

FIG. 6. Impact of the σ_{DY} model of anisotropic pressure on the compactness of an NS with the contribution of hyperons and the two different treatments of the speed of sound at high densities. We vary the values of Δ; those are -1.0, -2.0, -3.0, and -4.0. WH ($\Delta = -3.24$) and WHSS ($\Delta = -2.7$) are the compactness of $2.6M_\odot$ maximum NS mass. The orange shaded region shows the range of the maximum compactness of a heavy pulsar, that is, PSR J0348+0432 [28,164]. The green shaded region shows the highest maximum compactness of an NS up to now [165]. The highest maximum compactness of an NS is $C_{max} \simeq 0.35$.

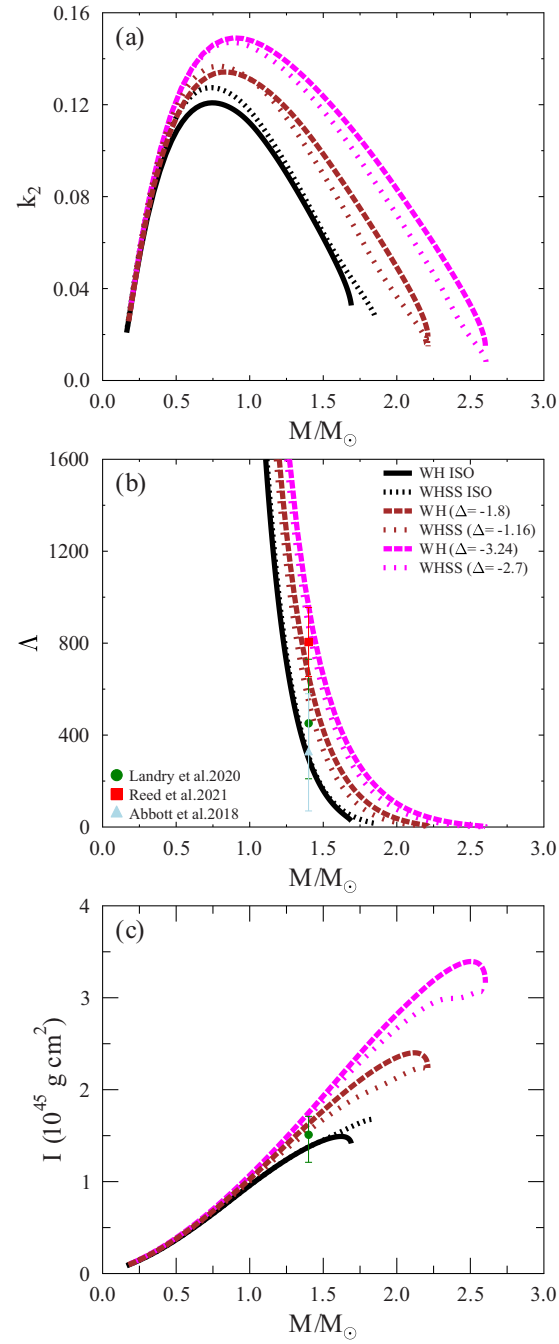

FIG. 7. Impact of the σ_{DY} model of anisotropic pressure on the tidal deformability of an NS and the moment of inertia of an NS with the contribution of hyperons and the treatment of the speed of sound. WH ($\Delta = -1.8$) and WHSS ($\Delta = -1.16$) are EOSs that are compatible with the maximum mass constraint from Ref. [49]. WH ($\Delta = -3.24$) and WHSS ($\Delta = -2.7$) show $2.6M_\odot$ maximum mass of NSs. We include constraints in Ref. [43] in panels (b) and (c) and include the constraint taken from Refs. [36,41] in panel (b).

higher depending on the Δ value than that of an isotropic NS. For an isotropic NS, the impact of the conformal bound on the sound speed produces a slightly higher k_2 peak than that without the conformal bound. However, in an anisotropic NS, the EOS with the conformal bound does not provide a pronounced impact on the k_2 peak. As k_2 is sensitive to Y and the compactness of the NS, it is evident in the panels (a) and (b) of Fig. 8 that Y and the compactness of the NS are responsible for the k_2 peak. Note that Y is a solution of Eq. (27) evaluated at $r = R$. The impact of the strength of anisotropic pressure through variation of the Δ value on tidal deformability Λ for the same NS mass is made by shifting Λ to a more considerable value compared to that of an isotropic NS, as can be seen in panel (b) of Fig. 7. However, the impact of the conformal bound on the EOS on the Λ trend is not significantly apparent for either an isotropic or an anisotropic NS with the variation of Δ value. As Λ is sensitive to k_2 and the compactness of the NS, it is evident in the bottom panel of Fig. 8 that the compactness is the reason for the insignificant difference in tidal deformability for either an isotropic or an anisotropic NS, and k_2 is the reason for a significant shift in the tidal deformability between the isotropic NS and anisotropic NSs.

In panel (c) in Fig. 7, we show the NS moment of inertia predicted by isotropic and anisotropic NSs. After the mass is larger than one solar mass, the anisotropic pressure impact on the moment of inertia appears to become significant for large NS masses. Thus, the impact of the conformal bound in the sound speed appears at high densities (large NS mass). Furthermore, the moment of inertia of the NS is sensitive to the mass and radius of the NS, due to the $I \sim MR^2$ relation. Therefore, the conformal bound impact on the sound speed requirement in the isotropic NS gives a larger moment of

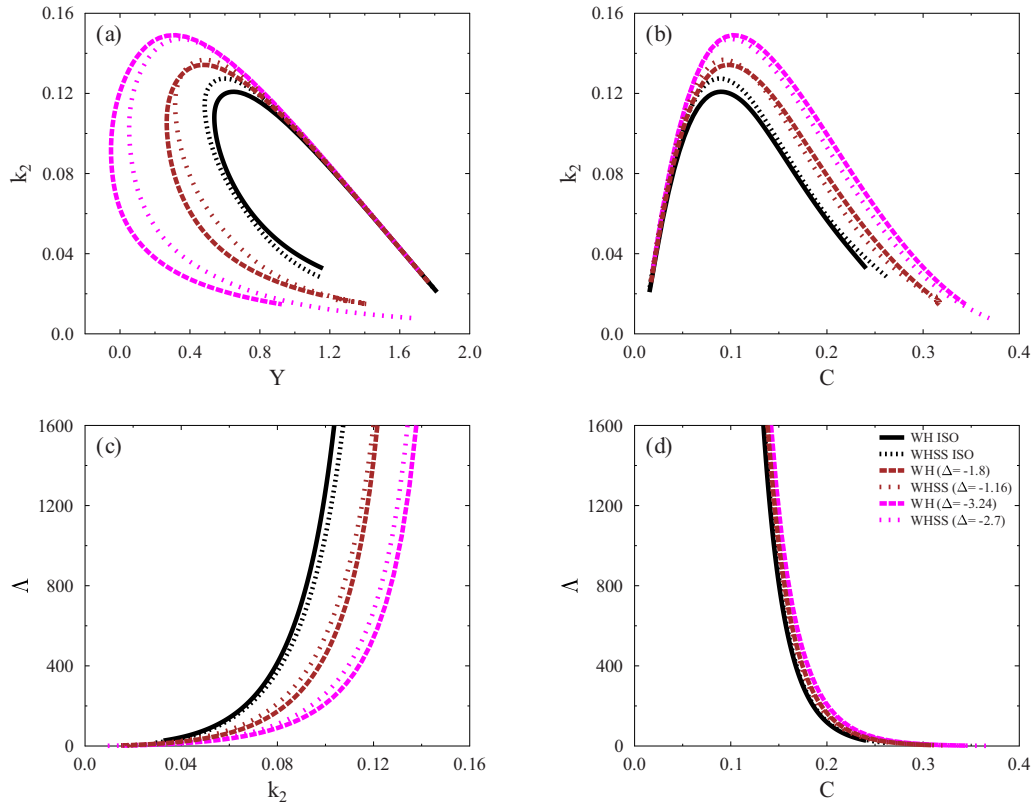

FIG. 8. The top panel shows k_2 as function of (a) Y and (b) NS compactness. The bottom panel shows the tidal deformability of NS as a function of (c) k_2 and (d) NS compactness. WH ($\Delta = -1.8$) and WHSS ($\Delta = -1.16$) are EOSs that compatible with the maximum mass constraint from Ref. [49]. WH ($\Delta = -3.24$) and WHSS ($\Delta = -2.7$) show $2.6M_\odot$ maximum mass of an NS.

inertia than that without considering this effect due to the mass of the NS. Its impact is opposite to that of anisotropic NSs.

In panels (b) and (c) of Fig. 7, we can compare the results with the observation data of the $1.4M_\odot$ NS tidal deformability and moment inertia ranges taken from Landry *et al.* [43], the ones from a recent analysis of the implication of the ^{208}Pb skin thickness measurement of PREX-II by Reed *et al.* [41], and one from the GW170817 event [36]. It is evident from Fig. 7 that the $1.4M_\odot$ NS tidal deformation predicted by the DY model if the mass can reach $2.6M_\odot$ [WH ($\Delta = -3.24$) and WHSS ($\Delta = -2.7$) EOSs] are closer to the range obtained in Ref. [41] than that of Refs. [36,43]. For one of the isotropic and anisotropic DY models with EOS WH ($\Delta = -1.8$) and WHSS ($\Delta = -1.16$), the tidal deformation is compatible to the one obtained in Refs. [43] and [36]. Moreover, the moment of inertia of a $1.4M_\odot$ NS for the isotropic and anisotropic DY models with EOS WH ($\Delta = -1.8$) and WHSS ($\Delta = -1.16$) is compatible with the constraint obtained in Ref. [43].

In conclusion, except for the slight deviation from the restricted range of canonical mass-radius from Breschi *et al.* [42] for the case the DY anisotropic model with $\Delta = -1.8$, the predicted NS maximum mass, $1.4M_\odot$, NS radius, moment inertia, and tidal deformation are compatible with the recently deduced observation and experimental data of Refs. [33,34,41,43,49]. Furthermore, these constraints [33,34,41,43,49] indicate that the compact object with mass around $2.6M_\odot$ observed as the secondary object from the GW190814 event is unlikely to be an anisotropic NS.

V. SUMMARY

In summary, we systematically investigate the mass-radius relation, the moment of inertia, and the tidal deformability of an anisotropic NS with hyperons predicted by the DY model [51]. We use a refined EOS and compare the results with recent constraints from multimessenger observation data analysis. Furthermore, we also study the possibility that the $2.6M_\odot$ massive object observed by the GW190814 event can be considered an anisotropic NS. We applied the EOS with the conformal bound on sound speed at high densities and implemented the SU(3) prescription in the hyperon sector, making the anisotropic NS relatively compact. We compared the nuclear matter properties predicted by the G3 parameter set with the ones predicted by the BSP, TM1e, FSUGarnet, and FSU2H parameter sets. We also compared the nuclear matter predicted by the G3 parameter set with other theoretical calculations and experimental constraints. We found that the G3 parameter set is quite representative to describe the NS EOS. We also compared the NS property results of the DY anisotropic model with the isotropic model and other anisotropic models. We have found results similar to the ones obtained in Ref. [82]. The predictions of the DY anisotropic model for WH EOS with $\Delta = -1.8$ are more compatible

than other anisotropic models with recent constraints from multimessenger observations data analysis [33,34,41–43,49]. It means that the constraints prefer an EOS without applying the conformal bound in the speed of sound. The parameter value of the DY model should be increased to $\Delta = -2.7$ for WH and $\Delta = -3.24$ for WHSS to yield a maximum mass of around $2.6M_{\odot}$. However, these multimessenger constraints [33,34,41,43,49] inform us that the compact object with a mass around $2.6M_{\odot}$, observed as the secondary object from the GW190814 event, is not likely an NS within the anisotropic pressure model.

ACKNOWLEDGMENT

A.S. is partially support by DRPM UI's (Skema PPI Q1 2021) Grant No. NKB-586/UN2.RST/HKP.05.00/2021.

[1] B. P. Abbott *et al.*, Astrophys. J. Lett. **896**, L44 (2020).
[2] I. A. Rather, U. Rahaman, V. Dexheimer, A. A. Usmani, and S. K. Patra, Astrophys. J. **917**, 46 (2021).
[3] E. R. Most, L. J. Papenfort, L. R. Weih, and L. Rezzolla, Mon. Not. R. Astron. Soc. **499**, L82 (2020).
[4] N. B. Zhang and B.-A. Li, Astrophys. J. **902**, 38 (2020).
[5] V. Dexheimer, R. O. Gomes, T. Klähn, S. Han, and M. Salinas, Phys. Rev. C **103**, 025808 (2021).
[6] I. A. Rather, U. Rahaman, M. Imran, H. C. Das, A. A. Usmani, and S. K. Patra, Phys. Rev. C **103**, 055814 (2021).
[7] S. Pinkanjanarod and P. Burikham, Eur. Phys. J. C **81**, 705 (2021).
[8] J. E. Horvath and P. H. R. S. Moraes, Int. J. Mod. Phys. D **30**, 2150016 (2021).
[9] A. Sedrakian, F. Weber, and J. J. Li, Phys. Rev. D **102**, 041301(R) (2020).
[10] V. B. Thapa and M. Sinha, Phys. Rev. D **102**, 123007 (2020).
[11] I. A. Rather, A. A. Usmani, and S. K. Patra, J. Phys. G: Nucl. Part. Phys. **48**, 085201 (2021).
[12] R. Somasundaram and J. Margueron, arXiv:2104.13612.
[13] R. Lobato *et al.*, J. Cosmol. Astropart. Phys. 12 (2020) 039.
[14] Z. Roupas, Astrophys. Space Sci. **366**, 9 (2021).
[15] F. J. Fattoyev, C. J. Horowitz, J. Piekarewicz, and B. Reed, Phys. Rev. C **102**, 065805 (2020).
[16] K. Huang, J. Hu, Y. Zhang, and H. Shen, Astrophys. J. **904**, 39 (2020).
[17] J. J. Li, A. Sedrakian, and F. Weber, Phys. Lett. B **810**, 135812 (2020).
[18] H. Tan, J. Noronha-Hostler, and N. Yunes, Phys. Rev. Lett. **125**, 261104 (2020).
[19] B. V. Lehmann, S. Profumo, and J. Yant, Mon. Not. R. Astron. Soc. **501**, 3727 (2021).
[20] R. Beradze and M. Gogberashvili, Mon. Not. R. Astron. Soc. **503**, 2882 (2021).
[21] H. C. Das, A. Kumar, B. Kumar, S. K. Biswal, and S. K. Patra, Int. J. Mod. Phys. E **30**, 2050088 (2021).
[22] C. Drischler, S. Han, J. M. Lattimer, M. Prakash, S. Reddy, and T. Zhao, Phys. Rev. C **103**, 045808 (2021).
[23] A. Kanakis-Pegios, P. S. Koliogiannis, and C. C. Moustakidis, Symmetry **13**, 183 (2021).
[24] P. Demorest, T. Pennucci, S. Ransom, M. Roberts, and J. Hessels, Nature (London) **467**, 1081 (2010).
[25] E. Fonseca, T. T. Pennucci, J. A. Ellis, I. H. Stairs, D. J. Nice, S. M. Ransom, P. B. Demorest, Z. Arzoumanian, K. Crowter, T. Dolch *et al.*, Astrophys. J. **832**, 167 (2016).
[26] Z. Arzoumanian *et al.*, Astrophys. J., Suppl. **235**, 37 (2018).
[27] H. T. Cromartie *et al.*, Nat. Astron. **4**, 72 (2019).
[28] J. Antoniadis *et al.*, Science **340**, 1233232 (2013).
[29] A. L. Watts *et al.*, Rev. Mod. Phys. **88**, 021001 (2016).
[30] S. Guillot *et al.*, Astrophys. J. Lett. **887**, L27 (2019).
[31] S. Bogdanov *et al.*, Astrophys. J. Lett. **887**, L25 (2019).
[32] S. Bogdanov *et al.*, Astrophys. J. Lett. **887**, L26 (2019).
[33] M. C. Miller *et al.*, Astrophys. J. Lett. **918**, L28 (2021).
[34] T. E. Riley *et al.*, Astrophys. J. Lett. **918**, L27 (2021).
[35] B. P. Abbott *et al.*, Phys. Rev. Lett. **119**, 161101 (2017).
[36] B. P. Abbott *et al.*, Phys. Rev. Lett. **121**, 161101 (2018).
[37] B. P. Abbott *et al.*, Phys. Rev. X **9**, 011001 (2019).
[38] B. P. Abbott *et al.*, Astrophys. J. Lett. **848**, L12 (2017).
[39] I. Arcavi *et al.*, Nature (London) **551**, 64 (2017).
[40] D. A. Coulter *et al.*, Science **358**, 1556 (2017).
[41] B. T. Reed, F. J. Fattoyev, C. J. Horowitz, and J. Piekarewicz, Phys. Rev. Lett. **126**, 172503 (2021).
[42] M. Breschi, A. Perego, S. Bernuzzi, W. D. Pozzo, V. Nedora, D. Radice, and D. Vescovi, Mon. Not. R. Astron. Soc. **505**, 1661 (2021).
[43] P. Landry, R. Essick, and K. Chatziioannou, Phys. Rev. D **101**, 123007 (2020).
[44] J. L. Jiang, S. P. Tang, Y. Z. Wang, Y. Z. Fan, and D. M. Wei, Astrophys. J. **892**, 55 (2019).
[45] Y. Lim, J. W. Holt, and R. J. Stahulak, Phys. Rev. C **100**, 035802 (2019).
[46] R. Essick, I. Tews, P. Landry, and A. Schwenk, Phys. Rev. Lett. **127**, 192701 (2021).
[47] G. Raaijmakers, S. K. Greif. K. Hebeler, T. Hinderer, S. Nissanke, A. Schwenk, T. E. Riley, A. L. Watts, J. M. Lattimer, and W. C. G. Ho, Astrophys. J. Lett. **918**, L29 (2021).
[48] P. T. H. Pang, I. Tews, M. W. Coughlin, M. Bulla, C. V. D. Broeck, and T. Dietrich, Astrophys. J. **922**, 14 (2021).
[49] A. Nathanail, E. R. Most, and L. Rezzolla, Astrophys. J. Lett. **908**, L28 (2021).
[50] E. Annala, T. Y. Gorda, E. Katerini, A. Kurkela, J. Nättilä, V. Paschalidis, and A. Vourinen, arXiv:2105.05132.
[51] D. Horvat, S. Ilijic, and A. Marunovic, Classical Quantum Gravity **28**, 025009 (2011).
[52] S. Chowdhury and T. Sarkar, Astrophys. J. **884**, 95 (2019).
[53] M. Moussa, Europhys. Lett. **117**, 49002 (2017).
[54] D. A. Terrero, V. H. Mederos, S. L. Pérez, D. M. Paret, A. P. Martínez, and G. Q. Angulo, Phys. Rev. D **99**, 023011 (2019).
[55] E. A. Becerra-Vergara, S. Mojica, F. D. Lora-Clavijo, and A. Cruz-Osorio, Phys. Rev. D **100**, 103006 (2019).
[56] S. L. Liebling and C. Palenzuela, Living Rev. Relativity **15**, 6 (2012).
[57] G. Raposo, P. Pani, M. Bezares, C. Palenzuela, and V. Cardoso, Phys. Rev. D **99**, 104072 (2019).
[58] A. Urbano and H. Veermäe, J. Cosmol. Astropart. Phys. 04 (2019) 011.
[59] M. Dutra, O. Lourenço, S. S. Avancini, B. V. Carlson, A. Delfino, D. P. Menezes, C. Providência, S. Typel, and J. R. Stone, Phys. Rev. C **90**, 055203 (2014).

[60] O. Lourenço, M. Dutra, C. H. Lenzi, C. V. Flores, and D. P. Menezes, Phys. Rev. C **99**, 045202 (2019).
[61] S. Weissenborn, D. Chatterjee, and J. Schaffner-Bielich, Nucl. Phys. A **881**, 62 (2012).
[62] S. Weissenborn, D. Chatterjee, and J. Schaffner-Bielich, Phys. Rev. C **85**, 065802 (2012); **90**, 019904(E) (2014).
[63] Y. Lim, C. H. Lee, and Y. Oh, Phys. Rev. D **97**, 023010 (2018).
[64] A. Sulaksono and B. K. Agrawal, Nucl. Phys. A **895**, 44 (2012).
[65] W. Z. Jiang, B. A. Li, and L. W. Chen, Astrophys. J. **756**, 56 (2012).
[66] N. Gupta and P. Arumugam, Phys. Rev. C **88**, 015803 (2013).
[67] M. Oertel, C. Providência, F. Gulminelli, and Ad. R. Raduta, J. Phys. G **42**, 075202 (2015).
[68] J. R. Torres, F. Gulminelli, and D. P. Menezes, Phys. Rev. C **95**, 025201 (2017).
[69] L. Tolos, M. Centelles, and A. Ramos, Astrophys. J. **834**, 3 (2017).
[70] T. T. Sun, S. S. Zhang, Q. L. Zhang, and C. J. Xia, Phys. Rev. D **99**, 023004 (2019).
[71] P. Ribes, L. Tolos, C. G. Boquera, and M. Centelles, Astrophys. J. **883**, 168 (2019).
[72] M. Fortin, Ad. R. Raduta, S. Avancini, and C. Providência, Phys. Rev. D **101**, 034017 (2020).
[73] S. K. Maurya, A. Banerjee, M. K. Jasim, J. Kumar, A. K. Prasad, and A. Pradhan, Phys. Rev. D **99**, 044029 (2019).
[74] J. M. Z. Pretel, Eur. Phys. J. C **80**, 726 (2020).
[75] L. Herrera and N. O. Santos, Phys. Rep. **286**, 53 (1997).
[76] A. Sulaksono, Int. J. Mod. Phys. E **24**, 1550007 (2015).
[77] A. M. Setiawan and A. Sulaksono, Eur. Phys. J. C **79**, 755 (2019); in *Proceedings of the 2nd International Symposium on Current Progress in Mathematics and Sciences 2016, 1–2 November 2016, Depok, Jawa Barat, Indonesia*, edited by T. Mart, D. Triyono, and K. A. Sugeng, AIP Conf. Proc. No. 1862 (AIP, New York, 2017), p. 030001.
[78] H. Abreu, H. Hernández, and L. A. Núñez, Classical Quantum Gravity **24**, 4631 (2007).
[79] H. Hernández, L. A. Núñez, and A. Vásquez-Ramírez, Eur. Phys. J. C **78**, 883 (2018).
[80] L. Herrera, E. Fuenmayor, and P. Leon, Phys. Rev. D **93**, 024047 (2016).
[81] M. Sharif and S. Sadiq, Eur. Phys. J. C **76**, 568 (2016).
[82] A. Rahmansyah, A. Sulaksono, A. B. Wahidin, and A. M. Setiawan, Eur. Phys. J. C **80**, 769 (2020).
[83] H. C. Silva, C. F. B. Macedo, E. Berti, and L. C. B. Crispino, Classical Quantum Gravity **32**, 145008 (2015).
[84] B. Biswas and S. Bose, Phys. Rev. D **99**, 104002 (2019).
[85] K. Yagi and N. Yunes, Phys. Rev. D **91**, 123008 (2015).
[86] G. Estevez-Delgado and J. Estevez-Delgado, Eur. Phys. J. C **78**, 673 (2018).
[87] P. S. Letelier, Phys. Rev. D **22**, 807 (1980).
[88] R. Rizaldy, A. R. Alfarasyi, A. Sulaksono, and T. Sumaryada, Phys. Rev. C **100**, 055804 (2019).
[89] M. D. Danarianto and A. Sulaksono, Phys. Rev. D **100**, 064042 (2019).
[90] A. Wojnar and H. Velten, Eur. Phys. J. C **76**, 697 (2016).
[91] J. Ovalle, Phys. Rev. D **95**, 104019 (2017).
[92] V. I. Afonso, G. J. Olmo, and D. Rubiera-Garcia, Phys. Rev. D **97**, 021503(R) (2018); V. I. Afonso, G. J. Olmo, E. Orazi, and D. Rubiera-Garcia, Eur. Phys. J. C **78**, 866 (2018).
[93] P. Nicolini, arXiv:1202.2102.
[94] M. Knipfer, S. Köppel, J. Mureika, and P. Nicolini, J. Cosmol. Astropart. Phys. 08 (2019) 008.
[95] T. Miyatsu, S. Yammamuro, and K. Nakazaki, Astrophys. J. **777**, 4 (2013).
[96] C. C. Moustakidis, T. Gaitanos, C. Margaritis, and G. A. Lalazissis, Phys. Rev. C **95**, 045801 (2017).
[97] C. Margaritis, P. S. Koliogiannis, and C. C. Moustakidis, Phys. Rev. D **101**, 043023 (2020).
[98] A. Kanakis-Pegios, P. S. Koliogiannis, and Ch. C. Moustakidis, Phys. Rev. C **102**, 055801 (2020).
[99] B. Reed and C. J. Horowitz, Phys. Rev. C **101**, 045803 (2020).
[100] J. B. Hartle, Phys. Rep. **46**, 201 (1978).
[101] S. Weinberg, *Gravitational and Cosmology: Principle and Applications of the General Theory of Relativity* (Wiley, New York, 1972), pp. 47–52.
[102] P. Bedaque and A. W. Steiner, Phys. Rev. Lett. **114**, 031103 (2015).
[103] J. M. Lattimer, in *Astrophysics and Cosmology: Proceedings of the 26th Solvay Conference on Physics*, edited by R. Blandford, D. Gross, and A. Sevrin (World Scientific, Singapore, 2014).
[104] I. Tews, J. Carlson, S. Gandolfi, and S. Reddy, Astrophys. J. **860**, 149 (2018).
[105] J. Alsing, H. O. Silva, and E. Berti, Mon. Not. R. Astron. Soc. **478**, 1377 (2018).
[106] L. McLerran and S. Reddy, Phys. Rev. Lett. **122**, 122701 (2019).
[107] N. Zhang, D. Wen, and H. Chen, Phys. Rev. C **99**, 035803 (2019).
[108] B. Kumar, S. K. Singh, B. Agrawal, and S. K. Patra, Nucl. Phys. A **966**, 197 (2017).
[109] B. K. Agrawal, A. Sulaksono, and P.-G. Reinhard, Nucl. Phys. A **882**, 1 (2012).
[110] H. Shen, F. Ji, J. Hu, and K. Sumiyoshi, Astrophys. J. **891**, 148 (2020).
[111] W.-C. Chen and J. Piekarewicz, Phys. Lett. B **748**, 284 (2015).
[112] R. L. Bowers and E. P. T. Liang, Astrophys. J. **188**, 657 (1974).
[113] M. Cosenza, L. Herrera, M. Esculpi, and L. Witten, J. Math. Phys. (NY) **22**, 118 (1981).
[114] M. Fortin, C. Providência, A. R. Raduta, F. Gulminelli, J. L. Zdunik, P. Haensel, and M. Bejger, Phys. Rev. C **94**, 035804 (2016).
[115] G. Baym, C. Pethick, and P. Sutherland, Astrophys. J. **170**, 299 (1971).
[116] G. Audi, A. H. Wapstra, and C. Thibault, Nucl. Phys. A **729**, 337 (2003).
[117] S. B. Rüster, M. Hempel, and J. Schaffner-Bielich, Phys. Rev. C **73**, 035804 (2006).
[118] M. Hempel and J. Schaffner-Bielich, J. Phys. G **35**, 014043 (2008).
[119] L. Guo, M. Hempel, J. Schaffner-Bielich, and J. A. Maruhn, Phys. Rev. C **76**, 065801 (2007).
[120] A. Pastore, D. Neill, H. Powell, K. Medler, and C. Barton, Phys. Rev. C **101**, 035804 (2020).
[121] N. Chamel, Phys. Rev. C **101**, 032801(R) (2020).
[122] F. Douchin and P. Haensel, Astron. Astrophys. **380**, 151 (2001).
[123] G. Baym, H. Bethe, and C. Pethick, Nucl. Phys. A **175**, 225 (1971).
[124] F. Grill, H. Pais, C. Providência, I. Vidaña, and S. S. Avancini, Phys. Rev. C **90**, 045803 (2014).

[125] F. Grill, C. Providência, and S. S. Avancini, Phys. Rev. C **85**, 055808 (2012).
[126] F. Ji, J. Hu, S. Bao, and H. Shen, Phys. Rev. C **100**, 045801 (2019).
[127] C. Mondal, X. Viñas, M. Centelles, and J. N. De, Phys. Rev. C **102**, 015802 (2020).
[128] G. A. Lalazissis, J. König, and P. Ring, Phys. Rev. C **55**, 540 (1997).
[129] C. J. Horowitz and J. Piekarewicz, Phys. Rev. Lett. **86**, 5647 (2001).
[130] N. K. Glendenning and S. A. Moszkowski, Phys. Rev. Lett. **67**, 2414 (1991).
[131] Y. Sugahara and H. Toki, Nucl. Phys. A **579**, 557 (1994).
[132] G. A. Lalazissis, T. Nikšić, D. Vretenar, and P. Ring, Phys. Rev. C **71**, 024312 (2005).
[133] S. Typel, G. Röpke, T. Klähn, D. Blaschke, and H. H. Wolter, Phys. Rev. C **81**, 015803 (2010).
[134] T. Gaitanos, M. Di Toro, S. Typel, V. Baran, C. Fuchs, V. Greco, and H. H. Wolter, Nucl. Phys. A **732**, 24 (2004).
[135] S. K. Dhiman, R. Kumar, and B. K. Agrawal, Phys. Rev. C **76**, 045801 (2007).
[136] B. K. Agrawal, Phys. Rev. C **81**, 034323 (2010).
[137] I. Vidaña and C. Providência, A. Polls, and A. Rios, Phys. Rev. C **80**, 045806 (2009).
[138] J. Carriere, C. J. Horowitz, and J. Piekarewicz, Astrophys. J. **593**, 463 (2003).
[139] A. Sulaksono and T. Mart, Phys. Rev. C **74**, 045806 (2006).
[140] B. A. Brown and A. Schwenk, Phys. Rev. C **89**, 011307(R) (2014); **91**, 049902(E) (2015).
[141] E. Khan, J. Margueron, and I. Vidaña, Phys. Rev. Lett. **109**, 092501 (2012).
[142] B. A. Li and X. Han, Phys. Lett. B **727**, 276 (2013).
[143] B. A. Li, Nucl. Phys. News **27**, 7 (2017).
[144] M. Oertel, M. Hempel, T. Klähn, and S. Typel, Rev. Mod. Phys. **89**, 015007 (2017).
[145] B. J. Cai and L. W. Chen, Nucl. Sci. Technol. **28**, 185 (2017).
[146] I. Tews, J. M. Lattimer, A. Ohnishi, and E. E. Kolomeitsev, Astrophys. J. **848**, 105 (2017).
[147] N. B. Zhang, B. J. Cai, B. A. Li, W. G. Newton, and J. Xu, Nucl. Sci. Technol. **28**, 181 (2017).
[148] T. Carreau, F. Gulminelli, and J. Margueron, Eur. Phys. J. A **55**, 188 (2019).
[149] C. Drischler, K. Hebeler, and A. Schwenk, Phys. Rev. C **93**, 054314 (2016).
[150] A. Le Févre, Y. Leifels, W. Reisdorf, J. Aichelin, and Ch. Hartnack, Nucl. Phys. A **945**, 112 (2016).
[151] P. Danielewicz, R. Lacey, and W. G. Lynch, Science **298**, 1592 (2002).
[152] S. K. Singh, S. K. Biswal, M. Bhuyan, and S. K. Patra, Phys. Rev. C **89**, 044001 (2014).
[153] S. Kubis and M. Kutschera, Phys. Lett. B **399**, 191 (1997).
[154] C. Drischler, J. W. Holt, and C. Wellenhofer, Annu. Rev. Nucl. Part. Sci. **71**, 403 (2021).
[155] N. Kaiser, Phys. Rev. C **103**, 054002 (2021).
[156] J. Schaffner-Bielich and A. Gal, Phys. Rev. C **62**, 034311 (2000).
[157] D. D. Doneva and S. S. Yazadjiev, Phys. Rev. D **85**, 124023 (2012).
[158] L. Herrera and W. Barreto, Phys. Rev. D **88**, 084022 (2013).
[159] T. Hinderer, Astrophys. J. **677**, 1216 (2008).
[160] B. Kumar, S. K. Biswal, and S. K. Patra, Phys. Rev. C **95**, 015801 (2017).
[161] T. Regge and J. A. Wheeler, Phys. Rev. **108**, 1063 (1957).
[162] K. Chakravarti, S. Chakraborty, S. Bose, and S. Sen Gupta, Phys. Rev. D **99**, 024036 (2019).
[163] J. B. Hartle, Astrophys. J. **150**, 1005 (1967).
[164] C. Palenzuela and S. L. Liebling, Phys. Rev. D **93**, 044009 (2016).
[165] J. M. Lattimer and M. Prakash, Phys. Rep. **442**, 109 (2007).